A simple model for low-frequency unsteadiness in shock-induced separation

S. PIPONNIAU, J. P. DUSSAUGE, J. F. DEBIÈVE AND P. DUPONT†

Institut Universitaire des Systèmes Thermiques Industriels
Université de Provence and UMR CNRS 6595, Marseille 13013, France

A model to explain the low-frequency unsteadiness found in shock-induced separation is proposed for cases in which the flow is reattaching downstream. It is based on the properties of fluid entrainment in the mixing layer generated downstream of the separation shock whose low-frequency motions are related to successive contractions and dilatations of the separated bubble. The main aerodynamic parameters on which the process depends are presented. This model is consistent with experimental observations obtained by particle image velocimetry (PIV) in a Mach 2.3 oblique shock wave/turbulent boundary layer interaction, as well as with several different configurations reported in the literature for Mach numbers ranging from 0 to 5.

1. Introduction

In many aeronautical applications, parameters of critical importance are imposed by unsteady conditions that can occur during flight, rather than steady conditions. Although these events are rare or do not contribute much to the local average energy, they can correspond to high local stress, which can affect the whole behaviour of the system. In supersonic flows, an important case occurs when unsteadiness involves shock waves producing locally large pressure fluctuations. They may act as strong aerodynamic loads and are felt along the whole flow downstream of the shock wave. This occurs in shock-induced separation, where low-frequency unsteadiness is produced. The separated region and the shock wave system that develops upstream of the separation line oscillate at low frequency, at least two orders of magnitude lower than the energetic scales present in the upstream boundary layer. For decades, the interaction with an incident shock and the compression ramp have been the two most documented cases (see Delery & Marvin 1986). A recent review of the main properties of these flows can be found in Dolling (2001). The origin of these low frequencies is not totally understood, and several models have been suggested to explain their development. A major problem is to separate the low-frequency shock motions, which appear when the flow is separating, from the motions related to unsteady conditions of the upstream boundary layer. This type of unsteadiness is typically based on upstream energetic scales and generate some corrugations of the shock wave (Debième & Lacharme 1985; Wu & Miles 2001; Garnier & Sagaut 2002). The associated frequency scales differ by two orders of magnitude from the low frequencies of the shock motions.

† Email address for correspondence: pierre.dupont@polytech.univ-mrs.fr

If pioneer works have been essentially experimental, modern numerical simulations have proved effective in simulating such flows (Garnier & Sagaut 2002), but the time integration was too short to allow capture of the low-frequency unsteadiness revealed by the experiments. Recently, significant improvements in the description of this low-frequency unsteadiness have been obtained, both from experimental works (Dupont, Haddad & Debiève 2006; Ganapathisubramani, Clemens & Dolling 2007*b*; Dupont *et al.* 2008; Souverein *et al.* 2008) and from numerical studies (de Martel, Garnier & Sagaut 2007; Wu & Martin 2007, 2008; Touber & Sandham 2008). These results confirm that in the shock wave boundary layer interactions under consideration (compression ramp or impinging shock wave) low-frequency movements of the separated region and motions of the shock wave formed upstream are observed. Nevertheless, there are still some discrepancies in the analysis of the results. Some researchers found that the low-frequency shock motions are related to unsteady aspects of the upstream boundary layer (Beresh, Clemens & Dolling 2002). They invoke the large streamwise vortices formed in the upstream boundary layer, with a very large longitudinal length scale. Such large scales have been observed both experimentally (Ganapathisubramani, Clemens & Dolling 2006) and numerically (Ringuette, Wu & Martin 2008) and seem to be similar to the superstructures observed in subsonic turbulent boundary layer (Kim & Adrian 1999; Adrian, Meinhart & Tomkins 2000). These superstructures can have a length of up to 30δ and could be a source of very low-frequency unsteadiness, in the range of frequency of the shock oscillations for some cases. Therefore, several attempts to correlate their dynamics with the shock unsteadiness and the separated bubble behaviour have been carried out. However, the results obtained appear to be contradictory. Ganapathisubramani, Clemens & Dolling (2007*a*); Ganapathisubramani *et al.* (2007*b*), using conditional analysis of their experimental observations, obtained evidence of strong links between upstream large scales and unsteadiness in the interaction in the case of a Mach 2 compression ramp flow. On the other hand, Dupont *et al.* (2006, 2008), in a Mach 2.3 incident shock wave interaction, and Wu & Martin (2008), in a Mach 2.9 compression ramp from direct numerical simulation (DNS) results, claimed that such a link was not significant in their results. For many years, several experimental works (Erengil & Dolling 1991*b*; Thomas, Putman & Chu 1994; Dupont *et al.* 2006, 2008) and more recently some numerical simulations, large-eddy simulation (LES) as well as DNS (Pirozzoli & Grasso 2006; Touber & Sandham 2008; Wu & Martin 2008), have shown that the dynamics of the separated bubble have to be related to the shock movements but without any certainty as to the source of the unsteadiness: do the shock movements influence the instantaneous position of the separated region through some upstream perturbations, or does the unsteadiness of the separated bubble impose the large motions of the shock? Phase relations between shock movements and separated bubble have been measured in experiments with compression ramps (Erengil & Dolling 1991*b*; Thomas *et al.* 1994) and with in incident shock wave configurations (Dupont *et al.* 2006; Debiève & Dupont 2007). The main result is the evidence that at low frequency pressure fluctuations at the foot of the shock and inside the separated bubble are out of phase. Negative lag times were obtained, but no clear convection process could be determined. Recently, Wu & Martin (2008) suggested that shock motions could be related to 'some feedback loop between the separation bubble, the separated shear layer and the separation bubble'. Finally, Dupont *et al.* (2006) have measured the characteristic frequency of shock motions in the case of a Mach 2.3 oblique shock wave for several angles of flow deflection ($7° < \theta < 9.5°$). Using a scaling derived from subsonic separated flows, initially proposed in Erengil & Dolling

(1991*b*), they found that for the same upstream turbulent boundary layer the shock frequency is directly related to the intensity of the interaction. They obtained a typical dimensionless frequency, or Strouhal number, based on the length of interaction L and on the velocity outside the separated bubble ($S_L = f L/U_1$) of about 0.03. These results suggest that the upstream perturbations cannot explain the time scale of the shock movements. Moreover, Dussauge, Dupont & Debiève (2006) have shown that this value of 0.03 gives a correct estimate of frequency in many cases, despite some scatter, and with a limited effect with regard to the Mach number, except for the Thomas's experiments (a compression ramp at Mach number 1.5). Thus, if the separated bubble is considered as a plausible source of shock unsteadiness, we have to consider the different time scales associated with its dynamics. Dupont *et al.* (2006) compared the longitudinal evolution of the wall pressure power spectral density (PSD) in an incident shock wave interaction as well as in a compression ramp interaction, with subsonic separated flows. They found similar spatial organizations, with the development of large structures in the first half of the bubble, which are shed into the downstream flow. Nevertheless, the characteristic frequencies cannot be directly compared, and the compressibility effects associated with the mixing layer have to be taken into account in order to relate the behaviour of subsonic separated bubbles to that of supersonic separated bubbles. These authors have also observed very low frequencies in the separated bubble, in the same range as for the shock motions, superimposed on fluctuations related to the large scales of the mixing layer. They have been associated to some large-amplitude oscillations of the bubble or flapping motions of the mixing layer (Dupont *et al.* 2008) as observed in subsonic separated flows. These bubble oscillations of large amplitude are correlated with the large longitudinal motions of the reflected shock. But an important difference between subsonic and supersonic characteristic frequency scales for the flapping motions is obtained. We just mentioned that a typical value of $S_L \simeq 0.03$ can describe qualitatively the shock motions in several experiments as well as in recent simulations (Touber & Sandham 2008; Wu & Martin 2008), whatever the geometry of the interaction. Nevertheless, a typical value of 0.12 is associated with the flapping of separated bubbles (Kiya & Sasaki 1983; Cherry, Hillier & Latour 1984); therefore there is at least a factor four between the two cases which is at present not understood. In this paper, we will propose to explain this fact through a simple analysis leading to define the main parametric dependence of this phenomenon, independent of the geometric conditions (compression corner, incident shock wave and the like) if the flow reattaches downstream. The model will be presented in §2, then compared in §3.1 with the experimental results obtained in a Mach 2.3 oblique shock wave/turbulent boundary layer interaction installed at the Institut Universitaire des Systèmes Thermiques Industriels (IUSTI). Finally, the parametric dependence will be checked versus the data available in the literature in §3.2.

2. Time scale of a separated bubble

2.1. *Aerodynamic scheme*

We propose here a simple analysis based on a global mass budget in the separated region. The aim is to build a scheme that can explain the breathing of the separated bubble when a turbulent boundary layer separates under the effect of an adverse pressure gradient. We will not, at this point, discuss how this gradient is generated (because of deceleration, shock wave interaction or any other reason). Nor will we consider the presence of a shock upstream of the bubble. We will concentrate on the
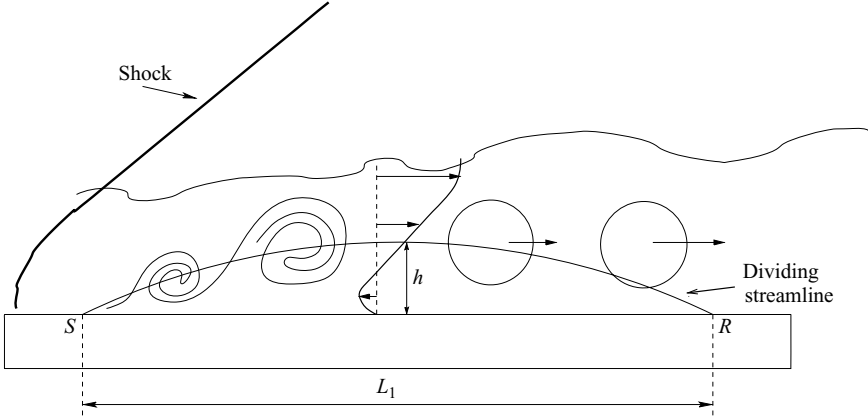
FIGURE 1. Sketch of the flow downstream of the reflected shock.

bubble itself. The separated zone is supposed to be of finite extent, with a spatial behaviour as summarized in figure 1. In the first part of the bubble, that is from the separation line, eddies are formed in the mixing layer zone and grow as it moves downstream. In a quasi-steady view, it may be assumed that fluid from the separated zone is entrained by the mixing layer. After some distance, these eddies are shed into the downstream flow, bringing with them their mass, momentum and vorticity outside the separated region. This generates, in the recirculating region, a default of mass that increases over time. Therefore, when the flow reattaches downstream, the mass amount inside the bubble decreases, and the steady separated situation cannot be maintained.

Consequently, there should be some flapping of the bubble which would let an air flux in the reverse direction occur with a time scale of T. The time scale required to entrain a significant amount of mass from the separated bubble obviously takes the form T = mass in the reverse flow/rate of mass entrainment. After a time of the order of T, there is a significant deficit of mass in the separation and a necessity to insure a new amount of reverse flow from the downstream region, thus allowing the process to be repeated. We propose that the resulting large movements of the bubble are at the origin of the large-amplitude shock motions. A similar scheme has already been proposed in both subsonic and supersonic cases (Cherry *et al.* 1984; Dandois, Garnier & Sagaut 2007; Wu & Martin 2008); here we propose to formulize it with simple hypotheses based on the dynamics of the equilibrium mixing layer. We will show that in shock-induced separated flows high convective Mach numbers can easily be produced and that this mechanism becomes highly sensitive to compressibility effects. Therefore, the model will be developed in as general a form as possible, taking into account possible density effects, with characteristic Mach numbers ranging from 0 to supersonic values.

2.2. Dimensional background

The spatial arrangement of a shock-induced separation can be sketched as in figure 1. This sketch corresponds to the incident oblique shock case. The incident shock wave and its reflection as an expansion are omitted. In the compression ramp case, the reattachment occurs generally downstream of the corner; nevertheless, the basic organization of the flow is similar to the sketch.

The basis of the model is to consider that the shed vortices bring with them a certain amount of mass that has to be reinjected in the bubble in order to maintain a mean separated region. The vortices are generated in the mixing layer that is formed downstream the separated shock (from line S), and the entrainment by the mixing layer produces a loss of mass in the recirculated zone. The high-velocity side of the layer is continuously fed and therefore is not affected by the mass ejection. On the low-velocity side, as the flow is reattaching, there is no source of mass to replace the amount of flow that is entrained by the mixing layer. Therefore, estimation of the time required to drain the initial bubble will be deduced from the entrainment rate of the low-velocity side of the mixing layer. In this work, we are looking at the order of magnitude of the time scale of the spreading of the bubble and the aerodynamic parameters that control it. Thus, several simplifying approximations are made, based on the classical properties of the plane mixing layer with variable density and/or compressibility effects. As the aim is to relate the mass swept along the mixing layer to the mass initially present in the mean recirculating bubble, we first evaluate this quantity, noted M_b. If we approximate the bubble by a triangle of length L_1 and of height h (see figure 1), with an average density of ρ_m, then we have by unit span

$$M_b = \frac{1}{2}\rho_m L_1 h. \qquad (2.1)$$

Here, h characterizes the height of the bubble. We will therefore define h as the maximum elevation of the dividing line defined as the set of points $\{y_j(x)\}$, where $\int_0^{y_j(x)} \rho u \, dy = 0$. In subsonic separated flows (Cherry *et al.* 1984) as well as in shock-induced separated flows (Dupont *et al.* 2006), the shedding of large structures that develop in the mixing layer occurs near of the middle of bubble, i.e. near $x = L_1/2$. Then, we can estimate the mass flux by unit span in the low-velocity part of the mixing layer by

$$M_{ej} = \int_{\delta_2(x=L_1/2)}^{y_0(x=L_1/2)} \rho u \, dy, \qquad (2.2)$$

where $\delta_2(x)$ is the edge of the mixing layer on the low-velocity side and $y_0(x)$ the centreline of the mixing layer. Moreover, M_{ej} involves only the low-velocity side of the mixing layer: in this region, the local Mach number is expected to be rather of limited value, and, in a first approximation, the density will be considered constant in this region and equal to the average density ρ_m. Thus, the characteristic time needed to entrain the initial mass is given by

$$T = \frac{M_b}{M_{ej}} = \frac{\frac{1}{2}L_1 h}{\int_{\delta_2(x=L_1/2)}^{y_0(x=L_1/2)} u \, dy}. \qquad (2.3)$$

It is obvious that the integral in the relation (2.3) can be related to the local thickness of the mixing layer (δ_ω) and to the shape of the velocity profile which is dependent on the external velocity at the high-velocity side u_1 and the velocity defect ΔU across the mixing layer zone. Then, characteristic frequency of the bubble can be estimated as

$$f = T^{-1} \propto \frac{\delta_\omega(x = L_1/2)\xi(u_1, \Delta U)}{\frac{1}{2}L_1 h}$$
$$\propto \delta_\omega' h^{-1}\xi(u_1, \Delta U),$$

where the ratio $\delta_\omega(x = L_1/2)/(L_1/2)$ is used as the local estimate of the spreading rate of the mixing layer $\delta'_\omega = \delta_\omega(x)/x$. Thus, the model leads to the definition of the characteristic Strouhal number of the breathing of the bubble due to mass entrainment inside the mixing layer region, based on the characteristic frequency $f = T^{-1}$, such as

$$S_h = \frac{fh}{u_1} = \delta'_\omega \zeta(u_1, \Delta U). \tag{2.4}$$

The relation (2.4) shows that the characteristic frequency of flapping must be related to the spreading rate of the mixing layer. This quantity is known to depend on the external velocity and density ratio across the mixing layer: respectively $r = u_2/u_1$ and $s = \rho_2/\rho_1$ (Brown & Roshko 1974). Moreover, Papamoschou & Roshko (1988) have shown that the spreading rate of the mixing layer is strongly dependent on compressibility effects, and they proposed the following expression:

$$\delta'_\omega = \frac{\delta'_{ref}}{2} \frac{(1-r)(1+\sqrt{s})}{1 + r\sqrt{s}} \Phi(M_c),$$

where $\delta'_{ref} \simeq 0.16$ is the spreading rate for subsonic half jet (see Browand & Troutt 1985) and M_c is the isentropic convective Mach number, defined by

$$M_c = \frac{\Delta U}{a_1 + a_2},$$

where a_i denotes the sound velocity. This leads to the final expression

$$S_h = \frac{fh}{u_1} = \Phi(M_c)g(r, s), \tag{2.5}$$

where $\Phi(M_c)$ is the normalized spreading rate and g is a function to be specified. Unfortunately, the quantity h is often not accessible in the literature, and the authors generally give only the length of separation of the bubble (L_1) or the length of interaction (L). Therefore, we have to introduce another Strouhal numbers based on these length scales:

$$S_l = \frac{fl}{u_1} = \Phi(M_c)g(r, s)\frac{l}{h}, \tag{2.6}$$

where l can be chosen as the separation length L_1 or the interaction length L. If the separation length is retained, L_1/h can be considered as the aspect ratio of the separated region. Unfortunately, this quantity is not well documented in the literature: in most of experimental works, only the length of interaction is available. In this case, the ratio L/h will be considered as a crude approximation of the real aspect ratio of the bubble. Thus, for a given L/h, similar influences of the Mach number can be expected for S_L and for S_h as will be shown in § 3.

The main result derived from relation (2.5) is the direct influence of the convective Mach number of the mixing layer through the function $\Phi(M_c)$. It is well known that this function is strongly Mach number dependent (see figure 2). This implies a substantial decrease in the Strouhal number S_L for convective Mach numbers up to 0.8. For higher convective Mach numbers, the function $\Phi(M_c)$ reaches a saturation level (about 0.2) which shows that constant value of S_L can be expected in this case. This could explain the large difference between the subsonic time scale ($S_L \simeq 0.12$; Kiya & Sasaki 1983) and the supersonic values when $M \geqq 2$ ($S_L \simeq 0.03$). Effectively, in shock-induced separated flows, an external Mach number larger than 2 leads to isentropic convective Mach number of the order of 1. For such high values, we
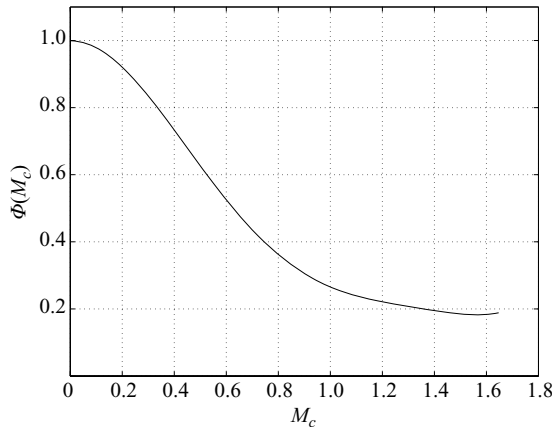
FIGURE 2. Normalized spreading rate as a function on the convective Mach number, adapted from Smits & Dussauge (2006).

have $\Phi(M_c = 1) \simeq 0.25$, which corresponds to the range of variation observed for the Strouhal number of the bubble breathing between subsonic and supersonic cases.

Relation (2.5) shows that the velocity and density ratios across the mixing layer must also be taken into account. In order to evaluate their influence and compare it with the drastic effects of the convective Mach number, we will now seek to evaluate the function $g(r, s)$ from classical similarity properties of the plane mixing layer. Therefore, a reasonable estimate of the integral of the relation (2.3) has to be obtained.

We will assume that self-similar velocity profiles describe the initial development of the mixing layer. Strictly speaking, an integration of velocity along the normal of the mixing layer axis should be performed. As the mean mixing layer makes an angle α with the wall, this can make a difference by a factor $\cos \alpha$. In the present analysis, where we are looking for parametric dependencies, such a refinement is ignored. As we want to estimate integral quantities in the final section of development of the mixing layer, such assumptions are not expected to be so restrictive. We consider the similarity variable η defined as

$$\eta = \frac{y - y_0(x)}{\delta_\omega(x)}.$$

Here, $\delta_\omega(x) = \delta_1(x) - \delta_2(x)$ is the local mixing layer thickness; the indices 1 and 2 refer respectively to the high- and low-velocity sides of the mixing layer; and $\delta_i(x)$ corresponds to the boundaries of the mixing layer on the high- and low-velocity side. Thus, the velocity profiles are approximated by the similarity relation

$$\frac{u - u_2(x)}{\Delta u} = F(\eta).$$

Therefore, expressed with the similarity variable η, the mixing layer profile extends from $\eta = -1/2$ to $\eta = 1/2$:

$$T = \frac{M_b}{M_{ej}} \simeq \frac{\frac{1}{2} L_1 h}{\delta_\omega(x = L_1/2) \int_{-\frac{1}{2}}^{0} u \, d\eta}.$$
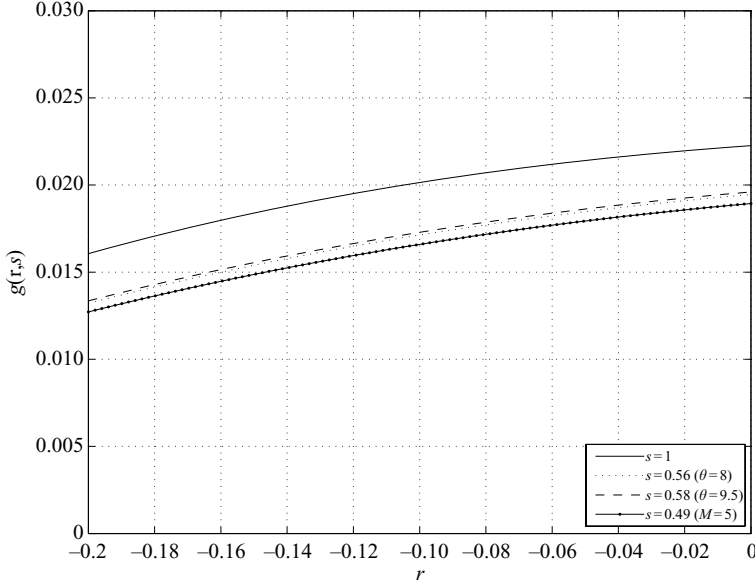
FIGURE 3. The function g for different density ratios.

Using the similarity relations in the previous definitions, we can rewrite relation (2.3) as

$$f = u_1 h^{-1} \delta'_\omega \left\{ (1-r)C + \frac{r}{2} \right\},$$

where $C = \int_{-\frac{1}{2}}^{0} F(\eta)\,d\eta$.

Finally, identifying the previous relation and the relation (2.5), we obtain

$$g(r,s) = \frac{\delta'_{ref}}{2} \frac{(1-r)(1+\sqrt{s})}{(1+r\sqrt{s})} \left\{ (1-r)C + \frac{r}{2} \right\}. \qquad (2.7)$$

To estimate the function g, it is necessary to specify the constant C. As a matter of fact, this integral quantity will depend slightly on the exact form of the velocity profile. In order to obtain a reasonable estimate, we can choose the similarity function $F(\eta)$ such as

$$F(\eta) = \frac{1}{2}\{1 + \mathrm{erf}(\sqrt{\pi}\eta)\}$$

where $\mathrm{erf}(\eta)$ is the error function. In this case, $C \simeq 0.14$.

To illustrate the influence of the velocity and density ratio, figure 3 plots the function $g(r,s)$ for typical domains of reverse flows and density ratios that can be expected in adiabatic conditions. The four cases under consideration correspond to the $M=2.3$ incident shock interaction of the IUSTI experiment for flow deviations of $8°$ and $9.5°$ (see the next section), to a Mach 5 compression ramp (Erengil & Dolling 1991b) and to a subsonic separated flow ($s=1$). The exact values of r and s are quite difficult to estimate, as the mixing layer boundaries can be only poorly defined. In order to obtain an estimate of these quantities in several cases, we chose to use the extreme values on both sides of the mixing layer. Therefore, u_1 and ρ_1 were set to the velocity and density values downstream of the separated shock outside the shear layer and u_2 and ρ_2 respectively to the maximum intensity of the reverse flow and the density at the wall. As shown in figure 3, the effects of the intensity of the reverse

M	Re_{δ_2}	U_∞	δ_0	δ_2	δ^*	H
2.28	5.1×10^3	550 ms^{-1}	11 mm	0.96 mm	3.4 mm	3.53

TABLE 1. Characteristics of the incoming turbulent boundary layer.
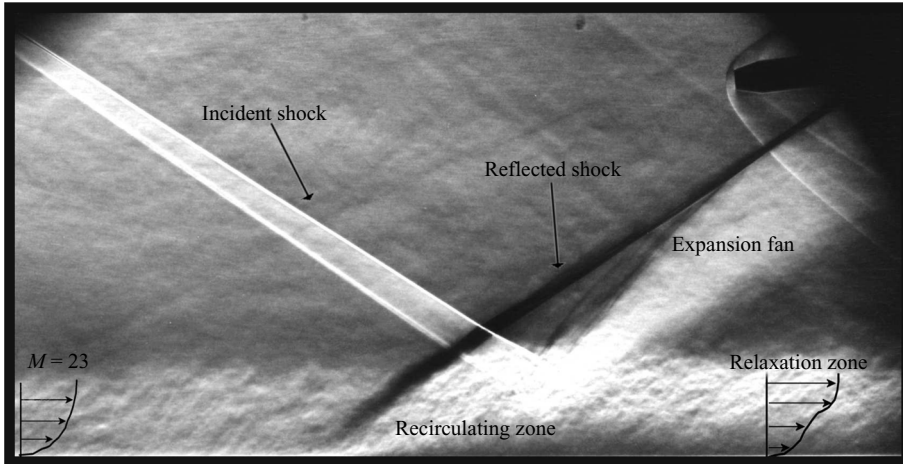
FIGURE 4. Spark Schlieren visualization of the interaction ($\theta = 8°$).

flow were rather limited, typically less than 30 %. The density effect in the range of Mach numbers considered here was of the same order as the effect of the intensity of the reverse flow and so was rather limited, compared with the reduction due to the convective Mach number.

3. Comparison with experimental observations

3.1. *The reflection case of IUSTI at M = 2.3*

3.1.1. *Experimental set-up*

The model presented in the previous section was compared to experimental results obtained in a Mach 2.3 oblique shock wave/turbulent boundary layer interaction. The flow has been already extensively documented (Dupont *et al.* 2005, 2006, 2008; Dussauge *et al.* 2006). The incoming boundary layer is turbulent fully developed. The main aerodynamic parameters are listed in table 1, where the thickness δ_0 was based on 99 % of the external velocity U_∞; δ^* is the displacement thickness; δ_2 is the momentum thickness; and H is the shape factor. A short time exposure Schlieren of the interaction is presented in figure 4.

The origin of the longitudinal coordinate x was fixed at the mean position (X_0) of the unsteady reflected shock. This position was derived from unsteady wall pressure measurements (Dupont *et al.* 2006). It was normalized by the length of interaction L defined as the distance between X_0 and the extrapolation down to the wall of the incident shock. The size of the interaction was 46 mm and 71 mm respectively for the 8° and the 9.5° cases. The dimensionless longitudinal coordinate $X^* = (x - X_0)/L$ was used to present the experimental results.

Velocity fields were obtained with particle image velocimetry (PIV) measurements. The PIV investigation was made using a Dantec Dynamics system. The light sheets

were generated by a double pulse Nd:Yag Laser New Wave Solo II, which delivered 30 mJ per pulse and separated in time by 1 μs, and the particle images were recorded by FlowSense cameras (1600×1200). Measurements were made in vertical planes, along the longitudinal axis of the wind tunnel, in order to characterize the velocity fields along the interaction. Because of the presence of the shock generator on the ceiling, some optical arrangements were necessary to illuminate the test section: a prism was placed into the diffuser to allow the laser sheet to propagate back to the measurement area. In order to perform conditional analysis of the velocity fields and to highlight the unsteady breathing of the bubble and its connection with the unsteady shock motions, sets of 5000 digital images were acquired. In the case of the $9.5°$ deflection, where the interaction grows significantly, two cameras were lined up next to each other in longitudinal direction to provide a wide field of view. The two pictures recorded by each camera were overlapped by about 10 %. A calibration grid was recorded, and the spatial correlation function between pictures gave spatial correspondences between both fields; a global panoramic picture was then created, covering an area of approximately 180×20 mm^2 ($\simeq 16\delta_0 \times 2\delta_0$). Incense smoke was used as seeding particles. The particles were injected from the wall upstream of the sonic section on the wind tunnel axis. As the wind tunnel stagnation pressure was less than atmospheric, the particles were naturally entrained into the flow. The time constant of the particles was estimated using PIV measurements of the mean velocity across the incident reflected shock outside the boundary layer. A time constant of 4.55 μs was deduced corresponding to diameters of 0, 5 μm (see Elena, Tedeschi & Gouin 1999). Samimy & Lele (1991) suggested that the particles accurately followed the velocity fluctuations in a turbulent mixing layer if the Stokes number $St = \tau_p/\tau_f$ with $\tau_f = \delta/U_\infty$ and τ_p the time response of the particles was less than about 0.5. In our experiments, the Stokes number is 0.23. This low value showed that the particles were able to follow the large-scale velocity fluctuations in the interaction (recirculation, mixing layer and the like). However, the shock still gave a drag of the particles. In our analysis, our intention was to measure not the absolute position of the shock but only the evolution of its position between several cases (see § 3.1.4). So it can be assumed that the seeding we are using was adapted to this study.

The images were processed using the Dantec software Flow Manager 4.71. For the wide field of view measurements, the calibration factor of the pictures was 17 pixels mm^{-1}. The intercorrelation was carried out recursively from a cell of size 128×64 to a final cell size of 32 pixels horizontally by 16 pixels vertically with a Gaussian weighting window applied to the interrogation cell. Therefore, the final effective cell size is 16×8 pixels; this led to a PIV resolution of 1×0.5 mm^2. An overlap of 75 % between cells provided a field of 390×80 vectors.

3.1.2. *Mean velocity fields*

The global organization of the interaction was illustrated for the $\theta = 9.5°$ case by maps of mean normal velocity and standard deviation of the normal velocity components (see figure 5). The mean dividing streamline was also reported on the maps.

The reflected shock was unsteady. This was clearly highlighted on the maps of the normal velocity standard deviation down to $y/\delta \simeq 0.5$. Just downstream of the foot of the shock, a high-turbulent-intensity region could be observed and associated with the development of the mixing layer. Its thickness was increasing continuously, up to $X^* \simeq 0.5$–0.6, where it reached a maximum level, and its downstream evolution was nearly parallel to the wall for large distances downstream of the interaction.
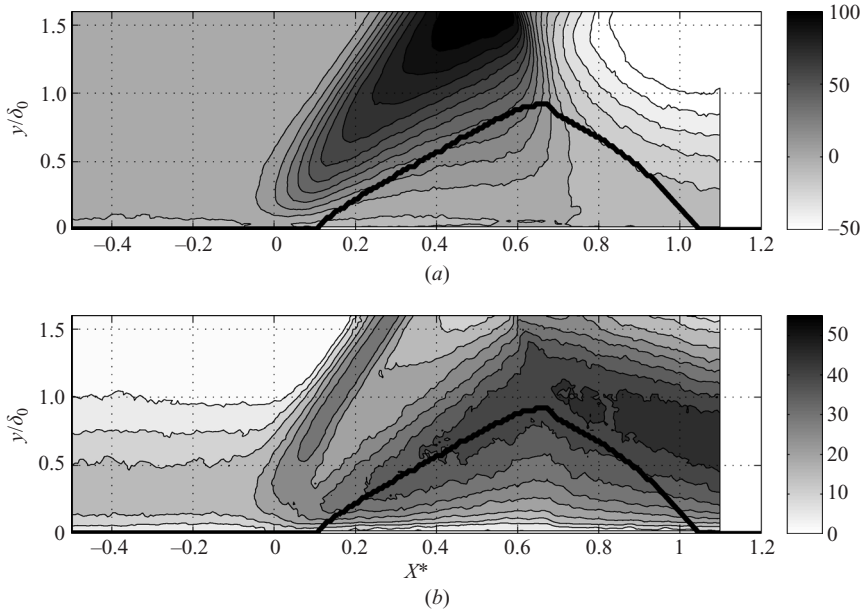
FIGURE 5. (*a*) Mean and r.m.s. (*b*) maps of the normal velocity in the interaction (ms^{-1}). The black line is the mean dividing streamline ($\theta = 9.5°$).

The region in which the mixing layer reached its maximum thickness was shown to correspond to the region in which large vortices that are shed downstream are created, as in subsonic separated flows (see Dupont *et al.* 2008). The model proposed in the previous section suggests that the mixing layer entrainment should control the low-frequency breathing of the separating region. To validate this hypothesis, conditional analyses of the instantaneous fields obtained by PIV were carried out.

3.1.3. *Conditional velocity fields*

Conditional analysis was applied to PIV velocity fields based on the instantaneous vertical extent of the recirculating region. The instantaneous dividing streamline was derived, and the unsteady recirculating bubble characteristics were sorted, from the instantaneous elevation of the bubble defined as $y_{i,max} = \max(y_j(x))$, where the instantaneous dividing line $y_j(x)$ was defined as in § 2.2. As already mentioned, the region of the flow in which the dividing streamline was estimated was a region of limited Mach number. Therefore, the density variations will be set aside, and the line will be approximated by $\int_0^{y_j(x)} u \, dy = 0$. These results were checked for their consistency with the determination that mean total enthalpy was supposed to be constant and where pressure was set constant in one section and equal to the wall pressure.

The probability density function (PDF) of $y_{i,max}$ in the 8° and 9.5° cases are shown in figure 6. As suggested by the model, large-amplitude movements were observed. We have selected three subsets of events:

   (*a*) shallow bubbles, $y_{i,max}/\delta_0 < y_1$;
   (*b*) medium bubbles, $y_2 < y_{i,max}/\delta_0 < y_3$;
   (*c*) thick bubbles, $y_4 < y_{i,max}/\delta_0$.

The values of y_i have been adjusted in such a way that each class represents about 10 % of the data. The corresponding subsets are in grey tint on the histograms (see
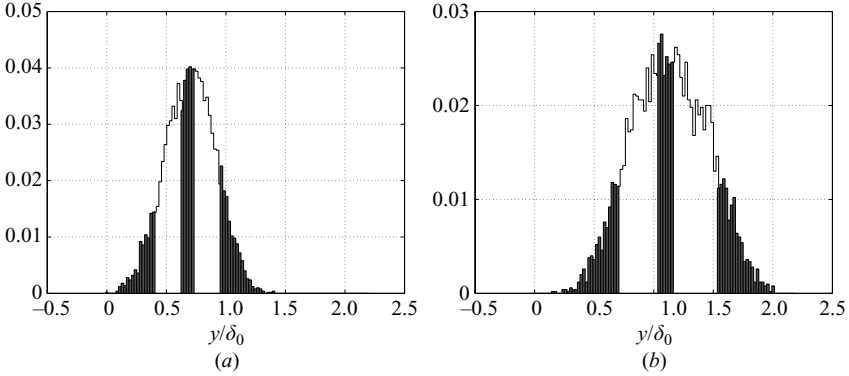
FIGURE 6. PDF of the instantaneous maximal elevation of the dividing streamline in the recirculating bubble: (a) $\theta = 8°$, (b) $\theta = 9.5°$.
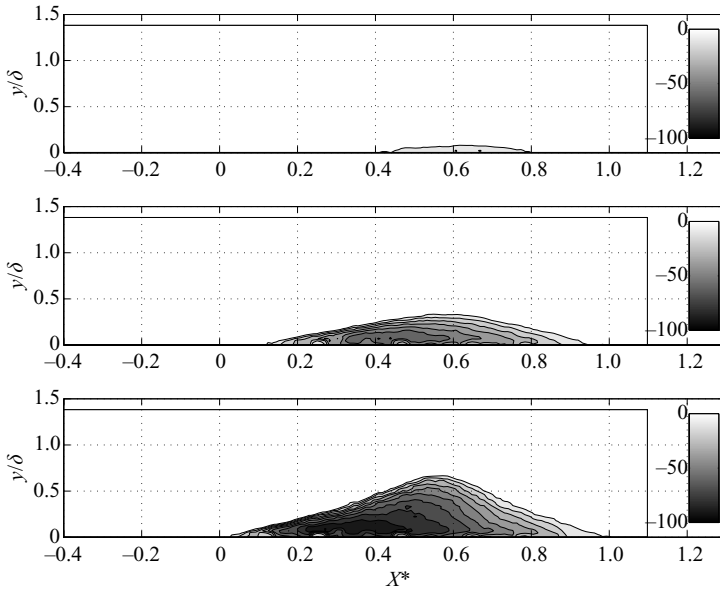

FIGURE 7. Conditional longitudinal velocity fields. Only negative velocities ranging between 0 and -100 ms^{-1} are shown; $\theta = 8°$.

figure 6). As we used 5000 fields to select the realizations, this gives roughly 500 samples for each subset. The corresponding conditional mean longitudinal velocity fields are reported in figure 7 for the 8° case and in figure 8 for the 9.5° case. To highlight the recirculating region, greyscale is limited to the null or negative velocities. This underlines the highly variable behaviour of the bubble.

As expected, the bubble can be nearly suppressed (at least in the 8° case), but this is an unsteady state, and therefore large injection of fluid, associated with large inflation of the bubble, can be observed with the same probability. Between these two extreme situations, the bubble experiences consecutive contractions and expansions. The very high intensity of the reverse flow should be noted in the cases of the thick bubbles: up to -100 ms^{-1} in the 8° case and up to -150 ms^{-1} in the 9.5° case, twice as large as the corresponding mean reverse flow velocity in both cases.
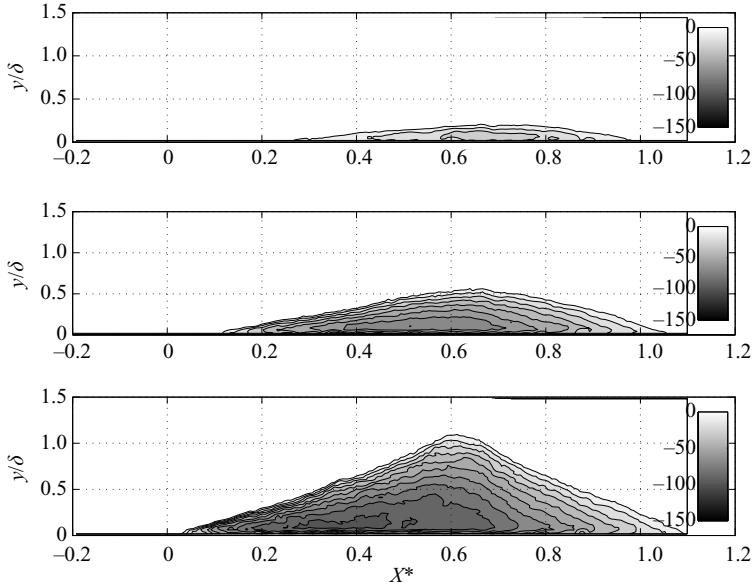
FIGURE 8. Conditional velocity fields. Only negative velocities ranging between 0 and $-150\ \mathrm{ms}^{-1}$ are shown; $\theta = 9.5°$.

3.1.4. *Links with shock movements*

For the same subsets of realizations, the conditionally averaged positions of the reflected shock have been estimated. We used the longitudinal evolution of the conditional normal velocity standard deviation ($\sqrt{\overline{v'^2}}$) to localize the median position of the shock. This is an efficient quantity to visualize the shock position (see figure 5b). We used the same procedure as for root mean square (r.m.s.) wall pressure measurements (see Dupont *et al.* 2006): the mean position of the reflected shock oscillations in the field are deduced from the longitudinal evolution of the transverse velocity fluctuations, applying a statistical scheme based on the presence of an unsteady shock. In this analysis, the median position of the reflected shock is associated with an extremum for the r.m.s. velocity.

Results for four vertical positions are reported in figure 9 for the 8° case and in figure 10 for the 9.5° case. Results confirmed the proposed scheme: the contractions of the bubble are related to downstream movements of the reflected shock, whereas the dilatations are related to reverse flow of very high intensity and consequently to upstream movements of the reflected shock. The amplitude of the conditionally averaged positions of the reflected shock remain in the same proportion, if compared to L, in the 8° and 9.5° cases ($\simeq 0.1L$).

Finally, an asymmetry in the shock motions can be remarked. The shock displacement downstream from its mean position remains limited during the bubble contraction. In contrast, during the large injection phase, the amplitude of the upstream shock motion is more than double. This is consistent with the proposed model: contractions of the bubble correspond to a progressive evolution related to the mass entrainment process, whereas the dilations correspond to a mass flux of large intensity in the reverse direction (up to 20%–25% of the external flow velocity). This behaviour is very similar to results from a DNS of a Mach 2.9 compression ramp
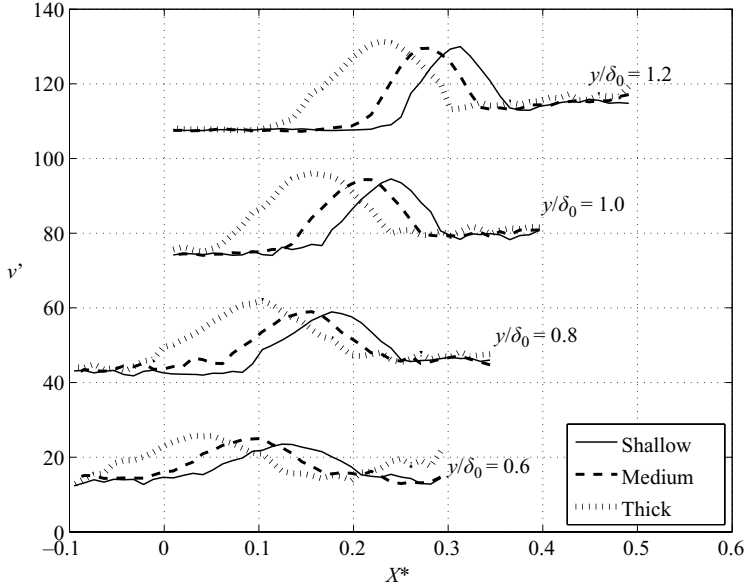
FIGURE 9. Conditional r.m.s. vertical fluctuations ($\theta = 8°$).
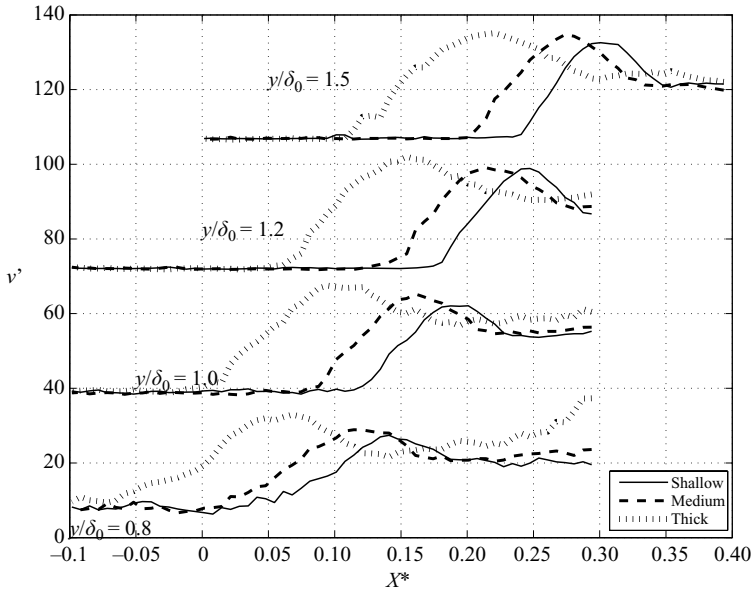
FIGURE 10. Conditional r.m.s. vertical fluctuations ($\theta = 9.5°$).

by Wu & Martin (2008), with shock motions correlated with low-frequency bubble unsteadiness.

The characteristic frequency of these large motions of the shock and of the bubble were derived from hot wire and unsteady wall pressure measurements in Dupont *et al.* (2006). It was defined by the maximum of the premultiplied spectra $fE(f)$. It is clear that the aim of (2.5) is to give the main parametric dependence of the frequency f and cannot be expected to give its absolute value with high accuracy.

θ	L (mm)	h (mm)	u_1	r	s	M_c	$\Phi(M_c)$	$g(r,s)10^{-2}$	$f(Hz)$	$f_{theo}(Hz)$
8.0°	46	5.5	505	−0.11	0.56	0.92	0.3	1.69	384	466
9.5°	71.5	10.2	490	−0.13	0.58	0.92	0.3	1.62	171	233

TABLE 2. Aerodynamic parameters of the separated bubble and Strouhal numbers of the shock motions from relation (2.5) and from experiments.

Nevertheless, it has to be able to give the right order of magnitude for f. In our experiments, the different quantities are available, and table 2 provides comparisons of the experimental results and the theoretical estimations.

Considering that several approximations have been made to derive the exact expression of the function $g(r,s)$ and that the height h is only used as a parameter to evaluate the initial mass inside the bubble, estimations of the bubble frequency f are of reasonable accuracy (+20 % and +36 % respectively for the 8° and 9.5° cases). Moreover, the decrease in the frequency with the shock intensity (−55 % from the experiments) is well captured by the model (−50 %). This confirms that the dramatic decrease in the Strouhal number S_L, with respect to the subsonic value (0.12), must be related to the large Mach dependence of the mixing layer entrainment through the function $\Phi(M_c)$ and that the time scale of the bubble breathing can be described by the model (relation (2.5)).

Nevertheless, we considered only one configuration (shock reflection) for one Mach number ($M = 2.28$). It is necessary, in order to evaluate the generality of the model proposed here, to compare its previsions with several other experiments involving different geometries and/or Mach numbers, with computations and other possible models. These comparisons are presented in the next section.

3.2. *Application of the model to several experiments of shock-induced separation*

Dussauge *et al.* (2006) proposed a compilation of the Strouhal number S_L for several data for separated flows available in the literature for Mach numbers ranging from 0 to 5, for compression ramps and shock reflection flows. We have adapted this compilation in figure 11. Here, $S_L = fL/U_1$, where U_1 is the velocity behind the separation shock and L is the length of interaction. For compression ramp cases, L is taken as the distance between the mean position of the foot of the shock and the reattachment point. Typical values around 0.03 are obtained for interactions at Mach numbers larger than 2, about four times lower than the Strouhal number observed in subsonic flows. An intermediate value was observed for moderate Mach number cases.

According to the relation (2.6), the characteristic flapping frequency of the mixing layer that develops downstream of the separated shock should be expressed by the classical Strouhal number $S_L = fL/U_1$ weighted by two functions: one that takes into account the density and reverse flow intensity effects ($g(r,s)$) and a second accounting for the effects of compressibility ($\Phi(M_c)$). Therefore, we estimated the quantity $S_L \times \{g(r,s)\Phi(M_c)\}^{-1}$ for the same flows. This quantity can also be considered as an estimation of the aspect ratio of the interaction L/h (see relation (2.6)). As mentioned in §2.2, the exact values of r and s are quite difficult to estimate. Therefore, in a way similar to our experimental results, u_1 and ρ_1 will be set to the velocity and density values downstream of the separation shock outside the shear layer. The reverse flow intensity is rarely given in the literature, but as shown in figure 3 this leads to limited correction. Therefore, when the reverse flow intensity is unknown, we set a value of

References	M	Re_δ ($\times 10^4$)	L (mm)	s	M_c	$\Phi(M_c)$	$g(r,s)$	S_L	$\dfrac{S_L/g(r,s)}{\Phi(M_c)}$
Kiya & Sasaki (1983)	0	/	200	1	0	1	0.02	0.12	5.96
Thomas *et al.* (1994)	1.5	18	30.3	0.85	0.49	0.63	0.019	0.1	8.29
Touber & Sandham (2008)	2.3	2.1	39	0.56	1	0.27	0.0132	0.0286	8.08
Wu & Martin (2008) (DNS) and Ringuette & Smits (2007) (experiment)	2.9	3.7	26.9	0.63	0.77	0.37	0.0177	0.036	5.47
Dolling & Brusniak (1989)	2.89	144	54	0.64	0.86	0.32	0.0113	0.025	6.85
Erengil & Dolling (1991*b*)	5	87	28	0.49	0.91	0.298	0.0166	0.03	6.06

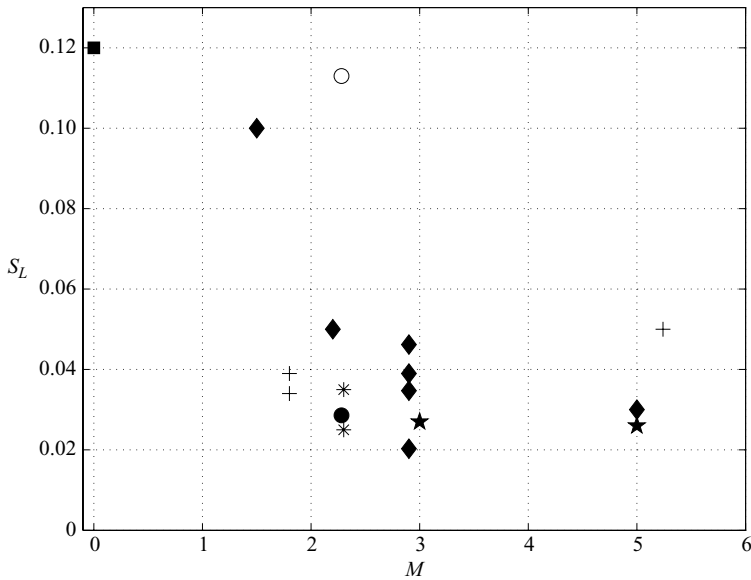TABLE 3. Aerodynamic parameters and Strouhal number for various cases.

FIGURE 11. Dimensionless frequency (S_L) of the shock oscillation in various configurations: (■) subsonic separation from Kiya & Sasaki (1983); (◆) compression ramp cases; (∗) IUSTI reflection cases; (+) overexpanded nozzle (restricted shock separation); (★) blunt fin; (●) Touber & Sandham (2008); (○) estimated superstructures upstream influence for the 8° IUSTI case. Adapted from Dussauge *et al.* (2006)

$r = -0.1$ which seems reasonable for many separated flows. To estimate the density near the wall inside the interaction, a hypothesis of constant total temperature across the layer is made once again, and we set aside the normal gradient of pressure across the layer. Even if this last hypothesis is not strictly verified for this non-parallel flow, it cannot generate strong deviation from the real value. These approximations are believed adequate for testing the parametric dependencies established in § 2.2. Table 3 shows the parameters and Strouhal number values used in available experimental or numerical works. The compilation is presented in figure 12.

Apart from the experimental data, we have also plotted the values of the Strouhal number corresponding to the superstructures for IUSTI flow conditions (see figure 11). We considered eddies as detected in experiments by Ganapathisubramani *et al.*

(2007a), with a typical length of $30\delta_0$, convected at a speed of $0.75U_e$. Only the value for a deflection of 8° has been considered: for $\theta = 9.5°$, the Strouhal number is 0.17, much higher than from all the other data, and for that reason it has not been retained. Moreover, we have reassessed the Strouhal number found in the LES simulations of Touber & Sandham (2008) for $\theta = 8°$, to use a normalization consistent with the definition in the present paper. The result agrees with the experimental value.

While there is still significant scatter, the experimental data from the subsonic case to the Mach 5 compression ramps in the range of a mean representative value of 6, $\pm 20\,\%$, except for the transonic case of Thomas *et al.* (1994), which is estimated around 8. The value corresponding to Touber & Sandham (2008) simulation is somewhat above the experimental value, because of discrepancies in the intensity of the computed reverse flow. As the original values of Strouhal numbers vary by a factor of four for these different cases, it is clear that the main effects due to the Mach number are conveniently described, as well as for the subsonic case ($S_L \simeq 0.12$) and for the higher Mach number cases ($2 < M < 5$, $S_L \simeq 0.03$).

4. Discussion and conclusions

Low-frequency unsteadiness in shock-induced separation has been considered. A simple scheme based on the entrainment properties of the mixing layer which develops at the edge of the separation is proposed to explain its origin in the cases in which the flow is reattaching downstream. The main parameters that influence the time scale are derived, in particular the dominant effect due to compressibility. This is related to large differences observed in low-frequency flapping in subsonic and supersonic separated flows. The experimental results obtained in the IUSTI incident shock wave reflection are in very good agreement with the proposed model, while the action of the superstructures on the interaction does not give an appropriate value for the characteristic frequency in this experiment. Similarly, the low-frequency shock unsteadiness observed in various shock-induced separation, experimentally or from recent DNS and LES, are very well estimated from the model for a wide range of Mach numbers, independent of the particular geometry of the flow. The large decrease of the Strouhal number for upstream Mach number ranging from 0 to 2 and saturation with a value of about 0.03 is well predicted; these are associated with the dramatic reduction of the compressible spreading rate of the mixing layer in this range of Mach numbers. Therefore, the main source of low-frequency unsteadiness in shock-induced separated flows seems clearly to be the dynamics of the separated bubble, at least in flows far enough from incipient separation, as in figure 1.

Another issue would be the generality of the present formulation. All the flows under consideration here refer to strong interactions in which mean separation is occurring. Recently, Humble *et al.* (2007) and Souverein *et al.* (2008) have performed advanced PIV experiments in a shock reflection at Mach 1.7 and 2, with flow deviation of 6° and 10°. These experiments correspond to incipient cases: there is no mean separation. Nevertheless, instantaneous flow fields have highlighted an intermittent development of bubbles of separated flow. Humble *et al.* (2007) made tomographic PIV measurements and have suggested that shock motions are related to structures of the upstream boundary layer. An attempt to characterize the time scale of the shock motions has been derived from dual PIV measurements (see Souverein *et al.* 2008). They used two consecutive velocity fields, separated by a tunable time delay varying from 5 to 2000 µs. For the reflected shock motions, they obtained significant autocorrelation values even for large delay times. Unfortunately, frequential
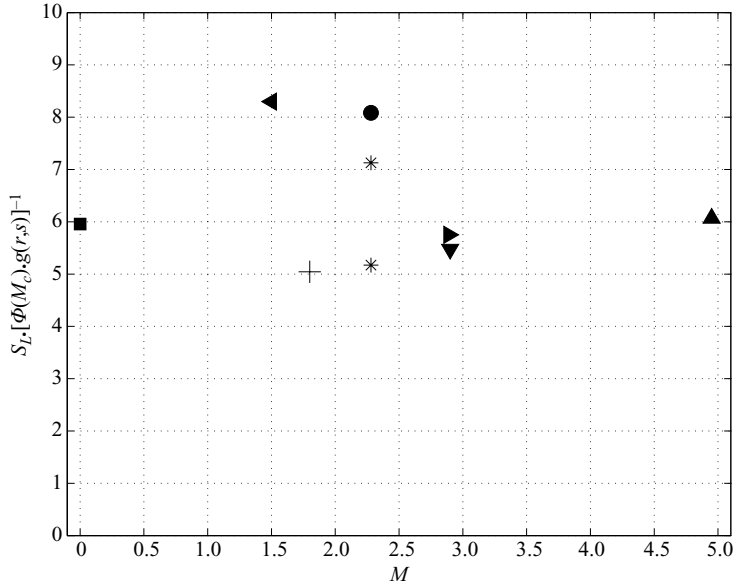
FIGURE 12. Dimensionless frequency of the shock oscillation normalized as suggested by relation (2.6): (■) subsonic separation from Kiya & Sasaki (1983); (∗) IUSTI's reflection cases; (◄) Thomas *et al.* (1994); (►)Dolling & Brusniak (1989); (▲) Erengil & Dolling (1991*a*); (▼) Wu & Martin (2008) (DNS) and Ringuette & Smits (2007) (experiment); (●) Touber & Sandham (2008).

analysis was not possible in their operating conditions. The IUSTI configuration was used to look for spectral information. The experiment was run at 5.5° flow deviation; this corresponds to incipient separation in our experimental conditions. The frequency of the shock motions has been determined from hot wire measurements. The premultiplied spectrum of the signal recorded in the vicinity of the mean position of the shock in the outer flow is reported in figure 13 together with the equivalent spectra obtained in the 8° and 9.5° cases. It is clear that the spectra are very different: in the separated cases, a low-frequency band is clearly dominant, while for the incipient separation, the spectrum extends from low frequencies to the cut off from the signal conditioner, with no maximum at low frequency. This is compatible with results obtained by Souverein *et al.* (2008). Therefore, it seems that low-frequency shock motions are closely related to the presence of a separated region downstream of the separation shock, at least for a shock reflection. Indeed, it seems likely that if the vertical extent h of the bubble becomes smaller with respect to the initial boundary layer thickness the dynamics of the separated bubble are significantly affected by the vicinity of the wall (see for example Simpson 1989). Consequently, the case of unsteadiness in incipient separation has to be considered with some care.

   Nevertheless, upstream influences cannot be completely ignored and must also be considered. Therefore, the same conditional analysis as in §3.1.3 has been made to check whether the breathing of the bubble and the reflected shock motion can be connected to events in the upstream boundary layer. The conditionally averaged velocity profiles were compared in a section upstream of zone in which the shock oscillates, for the subsets of realizations defined in figure 6. The conditional mean longitudinal velocity in the section $X^* = -0.45$ is reported in figure 14(*a*) for the 8° deviation and figure 14(*b*) for the 9.5° case. Only a very small modification of
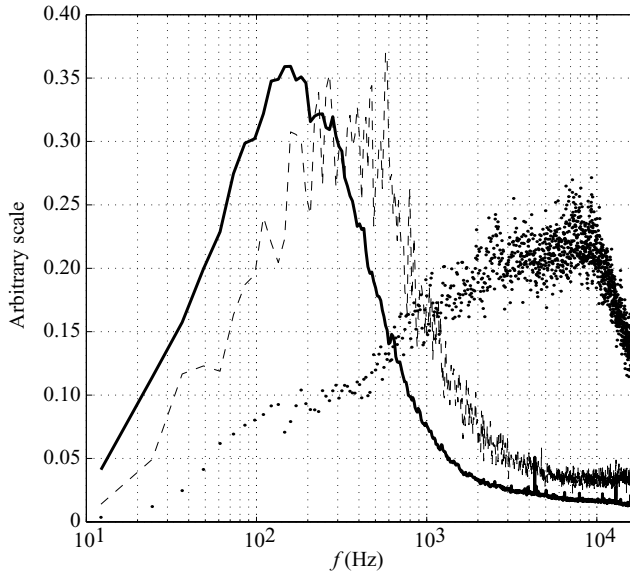
FIGURE 13. PSD of the unsteady reflected shock: (——) $\theta = 9.5°$; (- - -) $\theta = 8°$; ($\cdots$) $\theta = 5.5°$.

the profiles has been observed for the extreme bubble states: the large-amplitude motions of the bubble correspond to mean conditional longitudinal velocity profile with velocities slightly larger than the other events. This is very similar to the proposal by Ganapathisubramani *et al.* (2007*b*) for a Mach 2 compression ramp. However, the maximum differences between velocity profiles are 1 % for the 8° case and 2 % for the 9.5°: this is of the order of measurement accuracy. From several experimental studies, the order of magnitude of velocity difference between the superstructures with the other structures should be of the order of $\pm 2 u_\tau$ (Adrian *et al.* 2000; Ganapathisubramani *et al.* 2007*a*). In our case, as $u_\tau \approx 25$ ms^{-1}, we would expect conditional velocity variations of about 100 ms^{-1} or 20 % of the external velocity: this is one order of magnitude larger than the observed variations.

We also checked the conditional analysis for higher-order statistics, i.e. the Reynolds stresses. In figure 14(*c*) we present the conditional longitudinal intensity of turbulence profiles in the same section; again, no significant modification can be observed. Similar results were obtained in sections closer to the interaction, out of the domain of oscillations of the reflected shock. Therefore, small variations in the upstream conditions seem unlikely to be the main reason for the large-amplitude motions of the separated bubble. This is consistent with the following observation: in our experiments, the characteristic frequency of shock motions and separated bubbles are affected by the shock intensity and are not related directly to any time scale of the upstream boundary layer. Nevertheless, the slight dependence, if any, could indicate that if the characteristic time is imposed by the dynamics of the bubble itself as proposed here upstream perturbations can perhaps interfere with the development of the extreme states of the bubble, when mass balance is sufficiently far from equilibrium. This could generate the very slight dependence observed in our results, despite the lack of evidence of any significant coherence at low frequencies between the upstream boundary layer and the shock motions, as found by Thomas *et al.* (1994), Debiève & Dupont (2007) and Wu & Martin (2008).
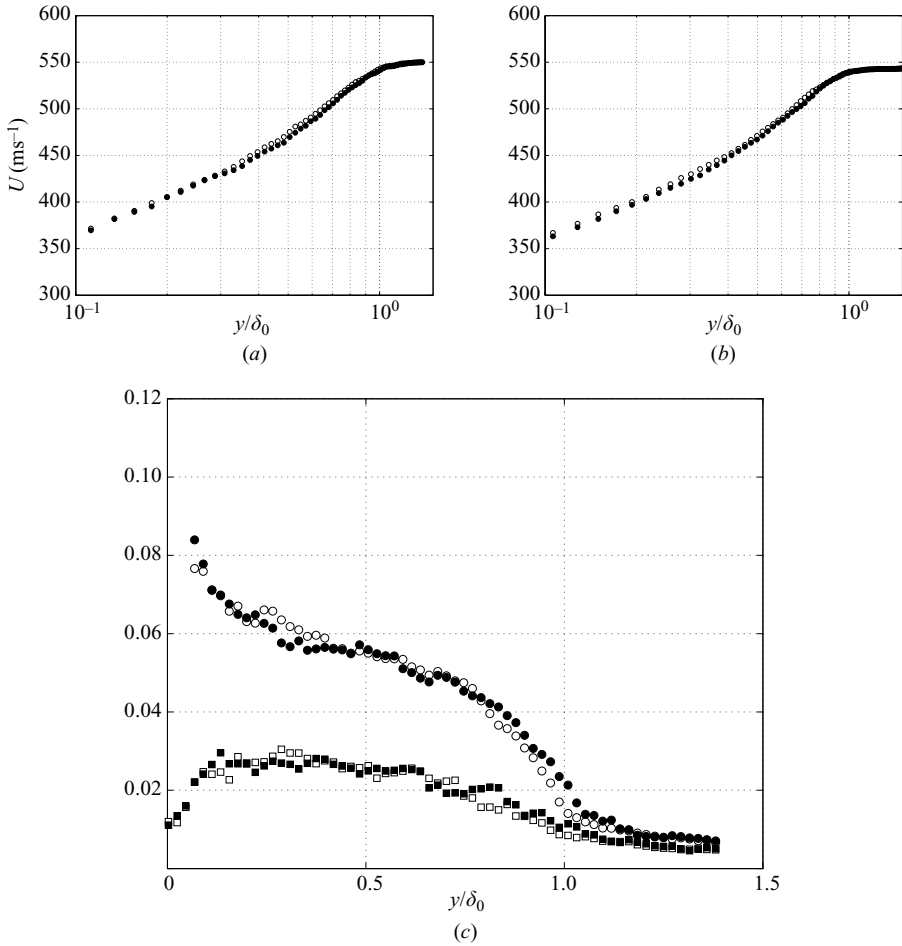
FIGURE 14. Conditional mean profiles in the upstream boundary layer in the section $X^* = -0.45$ (open symbols: shallow bubble; closed symbols: thick bubbles). (a) Longitudinal velocity, $\theta = 8°$; (b) longitudinal velocity, $\theta = 9.5°$; (c) ($\circ$) longitudinal u'/U_∞ and ($\square$) normal v'/U_∞ intensity of turbulence, $\theta = 8°$.

The success in collapsing the data set of flows with relation (2.6) for a wide range of Mach numbers (from 0 to 5) and a wide range of Reynolds numbers (Re_δ from 3.7×10^4 to 144×10^4) suggests that the geometry of flow configurations does not have much influence on the results. Moreover, the proposed scaling does not use directly upstream frequency scales, so the influence of the Reynolds number may appear only indirectly through the length scale h. This implies that, as supposed in the model, the initial development of the mixing layer defines the time constant of the bubble breathing and that the downstream history of the flow, in the vicinity of the reattachment line, is not a key factor in the unsteadiness of the interaction. A final result can be derived from the compilation reported in figure 14. As already mentioned, the quantity $S_L \times \{g(r, s)\Phi(M_c)\}^{-1}$ can be related to the aspect ratio of the interaction zone, L/h (see (2.6)). Therefore it seems that these different interactions have very similar aspect ratios, which is around 6. This result has been directly verified in our experiments in which the quantity h has been derived from the PIV data (see table 2). The experimental values are respectively 8.4 and 7 for the $8°$ and $9.5°$ cases.

However, the present model, which explicitly takes in account compressibility effects inside the separated bubble, gives a consistent and efficient way to represent shock unsteadiness in two-dimensional shock-induced separation for a wide range of Mach numbers.

REFERENCES

ADRIAN, R. J., MEINHART, C. D. S. & TOMKINS, C. D. 2000 Vortex organization in the outer region of the turbulent boundary layer. *J. Fluid Mech.* **422**, 1–53.

BERESH, S. J., CLEMENS, N. T. & DOLLING, D. S. 2002 Relationship between upstream turbulent boundary layer velocity fluctuations and separation shock unsteadiness. *AIAA J.* **40** (12), 2412–2422.

BROWAND, F. K. & TROUTT, T. R. 1985 The turbulent mixing layer: geometry of large vortices. *J. Fluid Mech.* **158**, 489–509.

BROWN, G. L. & ROSHKO, A. 1974 On density effects and large structures in turbulent mixing layers. *J. Fluid Mech.* **64**, 775–781.

CHERRY, N. J., HILLIER, R. & LATOUR, M. E. M. 1984 Unsteady measurements in a separated and reattaching flow. *J. Fluid Mech.* **144**, 13–46.

DANDOIS, J., GARNIER, E. & SAGAUT, P. 2007 Numerical simulation of active separation control by synthetic jet. *J. Fluid. Mech.* **574**, 25–58.

DEBIÈVE, J. F. & DUPONT, P. 2007 Dependence between shock and separation bubble in a shock wave/boundary layer interaction. In *IUTAM Symp. on Unsteady Separated Flows and Their Control*, Corfu, Greece.

DEBIÈVE, J. F. & LACHARME, J. P. 1985 A shock wave/free turbulence interaction. In *IUTAM Symp. on Turbulent Shear-Layer/Shock-Wave Interaction*, Palaiseau, France.

DELERY, J. & MARVIN, J. G. 1986 Shock wave–boundary layer interactions. *Tech Rep*. NATO. AGARDOgraph n°280.

DOLLING, D. S. 2001 Fifty years of shock-wave/boundary-layer interaction research: what next? *AIAA J.* **39** (8), 1517–1531.

DOLLING, D. S. & BRUSNIAK, L. 1989 Separation shock motion in fin, cylinder, and compression ramp-induced turbulent interactions. *AIAA J.* **27** (6), 734–742.

DUPONT, P., HADDAD, C., ARDISSONE, J. P. & DEBIÈVE, J. F. 2005 Space and time organisation of a shock wave/turbulent boundary layer interaction. *Aerosp. Sci. Technol.* **9** (7), 561–572.

DUPONT, P., HADDAD, C. & DEBIÈVE, J. F. 2006 Space and time organization in a shock induced boundary layer. *J. Fluid Mech.* **559**, 255–277.

DUPONT, P., PIPONNIAU, S., SIDORENKO, A. & DEBIÈVE, J. F. 2008 Investigation of an oblique shock reflection with separation by PIV measurements. *AIAA J.* **46** (6).

DUSSAUGE, J. P., DUPONT, P. & DEBIÈVE, J. F. 2006 Unsteadiness in shock wave boundary layer interaction with separation. *Aeros. Sci. Technol.* **10**, 85 –91.

ELENA, M., TEDESCHI, G. & GOUIN, H. 1999 Motion of tracer particles in supersonic flows. *Exp. Fluids* **26** (4), 288–296.

ERENGIL, M. E. & DOLLING, D. S. 1991*a* Correlation of separation shock motion with pressure fluctuations in the incoming boundary layer. *AIAA J.* **29** (11), 1868–1877.

ERENGIL, M. E. & DOLLING, D. S. 1991*b* Unsteady wave structure near separation in a Mach 5 compression ramp interaction. *AIAA J.* **29** (5), 728–735.

GANAPATHISUBRAMANI, B., CLEMENS, N. T. & DOLLING, D. S. 2006 Large-scale motions in a supersonic turbulent boundary layer. *J. Fluid Mech.* **556**, 271–282.

GANAPATHISUBRAMANI, B., CLEMENS, N. T. & DOLLING, D. S. 2007*a* Effects of upstream boundary layer on the unsteadiness of shock-induced separation. *J. Fluid Mech.* **585**, 369–394.

GANAPATHISUBRAMANI, B., CLEMENS, N. T. & DOLLING, D. S. 2007*b* Effects of upstream coherent structures on low-frquency motion of shock-induced turbulent separation. In *45th AIAA Aerospace Sciences Meeting and Exhibit*, Reno, Nevada.

GARNIER, E. & SAGAUT, P. 2002 Large eddy simulation of shock/boundary layer interaction. *AIAA J.* **40** (10), 1935–1944.

HUMBLE, R. A., ELSINGA, G. E., SCARANO, F. & VAN OUDHEUSDEN, B. W. 2007 Investigation of the instantaneous 3D flow organization of a shock-wave/turbulent boundary layer interaction using tomographic PIV. *Paper* 2007-4112. AIAA.

KIM, K. C. & ADRIAN, R. J. 1999 Very large-scale motion in the outer layer. *Phys. Fluids* **11**, 417–422.

KIYA, M. & SASAKI, K. 1983 Structure of a turbulent separation bubble. *J. Fluid Mech.* **137**, 83–113.

DE MARTEL, E., GARNIER, E. & SAGAUT, P. 2007 Large eddy simulation of impinging shock wave/turbulent boundary layer interaction at $M = 2.3$. In *IUTAM Symp. on Unsteady Separated Flows and their Control*, Corfu, Greece.

PAPAMOSCHOU, D. & ROSHKO, A. 1988 The compressible turbulent shear layer: an experimental study. *J. Fluid Mech.* **197**, 453–477.

PIROZZOLI, S. & GRASSO, F. 2006 Direct numerical simulation of impinging shock wave/turbulent boundary layer interaction at $M = 2.25$. *Phys. Fluids* **18**, 065113. 1–17.

RINGUETTE, M. J. & SMITS, A. J. 2007 Wall-pressure measurements in a Mach 3 shock-wave turbulent boundary layer interaction at a DNS-accessible Reynolds number. In *37th AIAA Fluid Dynamics Conf. and Exhibit*, Miami, Florida.

RINGUETTE, M. J., WU, M. & MARTIN, M. P. 2008 Coherent structures in direct numerical simulation of turbulent boundary layers at Mach 3. *J. Fluid Mech.* **594**, 59–69.

SAMIMY, M. & LELE, S. K. 1991 Motion of particles with inertia in a compressible free shear layer. *Phys. Fluids* A **3**, 1915–1923.

SIMPSON, R. L. 1989 Turbulent boundary-layer separation. *Annu. Rev. Fluid Mech.* **21**, 205–234.

SMITS, A. J. & DUSSAUGE, J. P. 2006 *Turbulent Shear Layers in Supersonic Flow*, 2nd edn. AIP Press.

SOUVEREIN, L., VAN OUDHEUSDEN, B. W., SCARANO, F. & DUPONT, P. 2008 Unsteadiness characterisation in a shock wave turbulent boundary layer interaction through dual-PIV. In *38th Fluid Dynamics Conf. and Exhibit*, Seattle, Washington.

THOMAS, F. O., PUTMAN, C. M. & CHU, H. C. 1994 On the mechanism of unsteady shock oscillation in shock wave/turbulent boundary layer interaction. *Exp. Fluids* **18**, 69–81.

TOUBER, E. & SANDHAM, N. D. 2008 Oblique shock impinging on a turbulent boundary layer: low-frequency mechanisms. In *38th AIAA Fluid Dynamics Conf.*, Seattle, Washington.

WU, M. & MARTIN, M. P. 2007 Direct numerical simulation of supersonic turbulent boundary layer over a compression ramp. *AIAA J.* **45** (4), 879–889.

WU, M. & MARTIN, M. P. 2008 Analysis of shock motion in shock wave and turbulent boundary layer interaction using direct numerical simulation data. *J. Fluid Mech.* **594**, 71–83.

WU, M. & MILES, R. B. 2001 Megahertz visualization of compression-corner shock structures. *AIAA J.* **39** (8), 1542–1546.